Biophysics and Physicobiology

Regular Article

Rotational motion of rhodamine 6G tethered to actin through oligo(ethylene glycol) linkers studied by frequency-domain fluorescence anisotropy

Tetsuichi Wazawa[1,2], Nobuyuki Morimoto[2], Takeharu Nagai[1] and Makoto Suzuki[2]

[1]Department of Biomolecular Science and Engineering, Institute for Scientific and Industrial Research, Osaka University, Ibaraki, Osaka 567-0047, Japan
[2]Department of Materials Processing, Graduate School of Tohoku University, Sendai, Miyagi 980-8579, Japan

Investigation of the rotational motion of a fluorescent probe tethered to a protein helps to elucidate the local properties of the solvent and protein near the conjugation site of the probe. In this study, we have developed an instrument for frequency-domain fluorescence (FDF) anisotropy measurements, and studied how the local properties around a protein, actin, can be elucidated from the rotational motion of a dye tethered to actin. Rhodamine 6G (R6G) was attached to Cys-374 using newly-synthesized R6G-maleimide with three different oligo(ethylene glycol) (OEG) linker lengths. The time-resolved anisotropy decay of R6G tethered to G-actin was revealed to be a combination of the two modes of the wobbling motion of R6G and the tumbling motion of G-actin. The rotational diffusion coefficient (RDC) of R6G wobbling was ~0.1 ns⁻¹ at 20°C and increased with OEG linker length. The use of the three R6G-actin conjugates of different linker lengths was useful to not only figure out the linker length dependence of the rotational motion of R6G but also validate the analyses. In the presence of a cosolvent of glycerol, although the tumbling motion of G-actin was retarded in response to the bulk viscosity, the wobbling motion of R6G tethered to actin exhibited an increase of RDC as glycerol concentration increased. This finding suggests an intricate relationship between the fluid properties of the bulk solvent and the local environment around actin.

Corresponding author: Tetsuichi Wazawa, Department of Biomolecular Science and Engineering, The Institute of Industrial and Scientific Research, Osaka University, Mihogaoka 8-1, Ibaraki, Osaka 567-0047, Japan.
e-mail:wz8@sanken.osaka-u.ac.jp

Fluorescent probes in solution undergo rotational Brownian motion that is dependent on such conditions as the solvent fluid properties, local steric restrictions imposed on the probes, and their interactions with nearby molecules [1,2]. The rotational Brownian motion of fluorescent probes can generally be measured using steady-state or time-resolved fluorescence polarization techniques. Specifically, if a fluorescent dye is conjugated to a protein, fluorescence polarization measurements should provide insight into the properties of the local environment and structure near the conjugation site of the protein and their interactions with the surrounding molecules.

Solvent molecules, including water, that surround a protein participate in solvation and affect the thermodynamics and conformational dynamics of the protein [3–5]. Because these properties are very relevant to protein function and conformational stability, investigation of the solvation layer properties is likely to lead to a better understanding of how solvation affects the protein. The properties of the solvation layers around proteins have been experimentally investigated by techniques such as dielectric relaxation spectroscopy [6–10], pulsed-field gradient ¹H-NMR [11,12], magnetic relaxation dispersion [13], equilibrium dialysis [14], and neutron scattering [15].

Frequency-domain fluorescence (FDF) measurement is a technique to measure the time-resolved fluorescence decay and anisotropy [16,17]. In FDF measurements, a fluorescent sample is illuminated with intensity-modulated excitation

light, and the amplitude and phase of the fluorescence modulation are measured. The time-resolved fluorescence anisotropy data taken from a fluorophore tethered to a protein can be analyzed to determine the rotational motion, and this information is expected to provide insight into the properties of the solvation layers around the protein. Although the time-correlated single photon counting (TCSPC) method is used to measure time-resolved fluorescence, FDF measurement is very useful in some cases, such as experiments involving very low values of fluorescence anisotropy and kinetic measurements [16].

In this study, we have developed an FDF measurement system to investigate the time-resolved fluorescence anisotropy of a fluorescent dye, rhodamine 6G, tethered to actin. Actin, a cytoskeletal protein, is ubiquitous to eukaryotic cells and plays vital roles in cellular processes, such as cell division, intracellular transport, cell motility, and muscle contraction [18,19]. Actin polymerizes into filaments at high salt concentrations (e.g., >50 mM KCl) in the presence of ATP, whereas actin remains monomeric at low salt concentrations (e.g., <several mM KCl) [20]. Interestingly, in a previous dielectric relaxation spectroscopy study, we revealed that the hydration shell around F-actin contained a water component that exhibited a higher dielectric frequency than that of bulk or pure water [8]; this property is not typical for other proteins and many organic compounds [6,7,21]. Thus, it is of great interest to probe the solvation layers around actin using time-resolved fluorescence anisotropy measurements of a fluorophore tethered to actin. This paper describes the set-up of a high-precision FDF measurement system using a lithium-niobate (LN) waveguide light modulator and subsequently describes the evaluation of its performance using samples of rhodamine 6G (R6G) dissolved in glycerol/water mixtures. Thereupon, we delineate the results of FDF anisotropy measurements of R6G tethered to actin.

Materials and Methods

Chemicals

1,5-Diamino-3-monooxapentane (DMP; Cat# O0278), 1,8-diamino-3,6-dioxaoctane, (DDO; Cat# B1431) 1,11-diamino-3,6,9-trioxaundecane (DTU; Cat# D3664), N-succinimidyl 3-maleimidopropionate (SMP; Cat# S0427), and N,N'-diisopropylethylamine (DIPEA; Cat# D1599) were purchased from Tokyo Chemical Industry (Tokyo, Japan). 6-Carboxyrhodamine 6G succinimidyl ester (R6G-OSu; Cat# 342) was obtained from AAT Bioquest (Sunnyvale, CA, USA). Tris(hydroxymethyl)aminomethane) (Tris) and adenosine 5'-triphosphate (ATP) were from Wako Pure Chemical Industries (Osaka, Japan). 2-[4-(2-Hydroxyethyl)-1-piperazinyl]ethanesulfonic acid (HEPES) was from Dojindo (Kumamoto, Japan). All other chemicals were of reagent grade or higher and purchased from Wako Pure Chemical Industries, Nacalai Tesque (Kyoto, Japan) or Sigma-Aldrich (St. Louis, MO, USA).

Preparation of rhodamine 6G maleimides

A two-step method [11] was used to prepare thiol reactive derivatives of rhodamine 6G such that the fluorophore and a maleimidyl group were crosslinked through an oligo(ethylene glycol) (OEG) linker. In the first step, an amine-reactive dye was aminated through a reaction with an OEG diamine. In the second step, the aminated dye was converted into a maleimidyl derivative by reaction with SMP that contained a maleimide group and an N-hydroxysuccinimidyl ester group (NHS).

R6G-OSu dissolved in N,N'-dimethylacetamide (DMA) was reacted with a 10-fold molar excess of an OEG diamine (DMP, DDO, or DTU) over the dye for 20 min in the presence of 1% (v/v) DIPEA to produce a R6G-amine (Fig. 1A). The mixture was dried using a centrifuge evaporator, and the red residue was dissolved in pure water. The R6G-amine was isolated by reverse-phase chromatography with isocratic elution using a SunFire C18 column (5 μm, 19×100 mm; Waters, Milford, MA, USA) and a mobile phase of water-acetonitrile (75 : 25, 74 : 26, and 73 : 27, v/v, for R6G-OEG1-NH_2, R6G-OEG2-NH_2, and R6G-OEG3-NH_2, respectively; see below) containing 0.1% (v/v) trifluoroacetic acid (TFA) at a flow rate of 3 mL min⁻¹ at room temperature. The fraction containing R6G-amine was collected and dried by centrifuge evaporation. The liquid chromatography was performed on a 626 HPLC system (Waters). The R6G-amines produced from DMP, DDO, and DTU were denoted R6G-OEG1-NH_2, R6G-OEG2-NH_2, and R6G-OEG3-NH_2, respectively.

The R6G-amine was dissolved in DMA and mixed with a 5-fold molar excess of SMP in the presence of 1% (v/v) DIPEA (Fig. 1B). After a 20-min incubation, 1% (v/v) acetic acid was added, the mixture was dried, and then, the residue was dissolved in pure water. To isolate maleimide-functionalized R6G (R6G-maleimide), reverse-phase chromatography using the SunFire column was performed using isocratic elution with a mobile phase of water-acetonitrile (74 : 26, v/v) without TFA at a flow rate of 3 mL min⁻¹. The fraction containing R6G-maleimide was collected and dried by centrifuge evaporation. The R6G-maleimides produced from R6G-OEG1-NH_2, R6G-OEG2-NH_2, and R6G-OEG3-NH_2 were denoted R6G-OEG1-Mal, R6G-OEG2-Mal, and R6G-OEG3-Mal, respectively (Fig. 1C). The details of the reverse-phase chromatography are provided in Section S1 of the Supplementary Material.

Actin preparation

Chicken skeletal muscle actin was prepared according to ref [22]. Briefly, G-actin was extracted from an acetone powder preparation of pectoral muscle using an aqueous solution (pH 8.0) containing 2 mM Tris-HCl, 0.2 mM ATP, 0.1 mM $CaCl_2$, and 1 mM dithiothreitol (DTT). G-actin was purified through cycles of polymerization with high-ionic strength buffers (≥0.1 M KCl) and depolymerization with G-buffer (2 mM HEPES-KOH (pH 7.8) and 0.2 mM ATP)
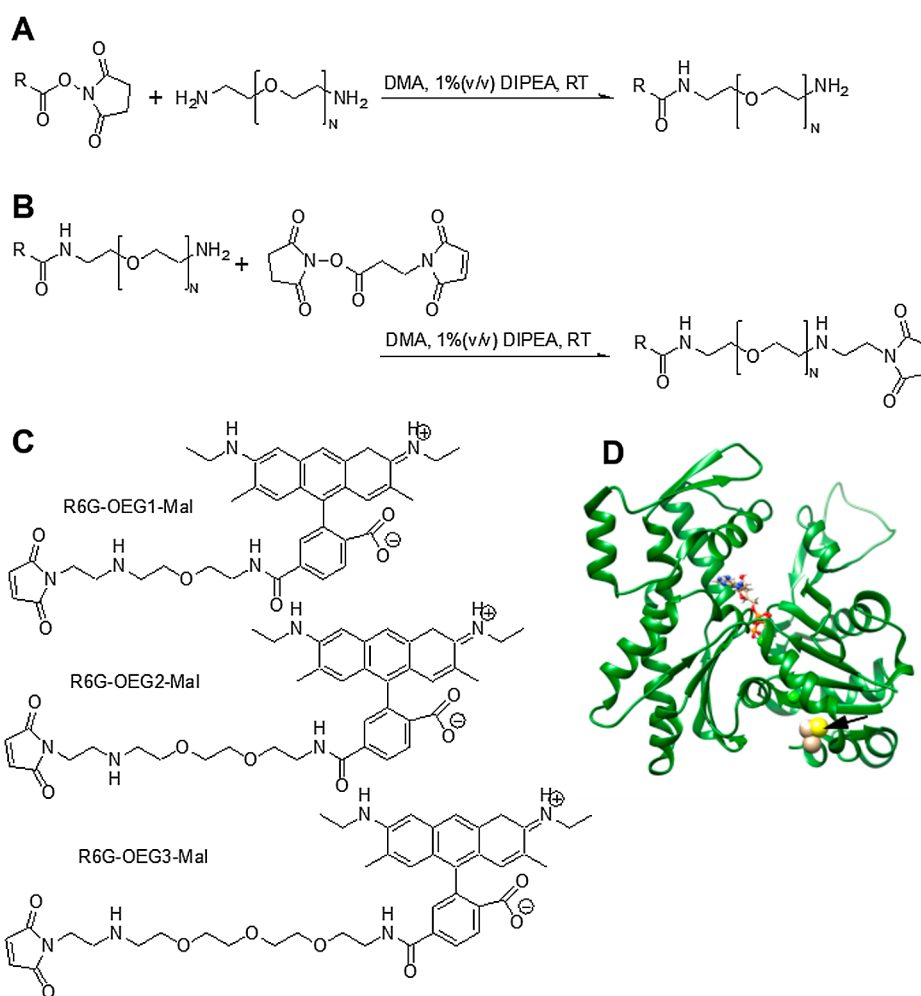
Figure 1 Reaction scheme of the synthesis of R6G maleimides and their chemical structures. (A) Reaction of R6G-OSu and diamino oligo(ethylene glycol) to produce R6G-amine. (B) Reaction of R6G-amine and SMP to produce R6G-maleimide. (C) Chemical structures of R6G-OEG1-Mal, R6G-OEG2-Mal, and R6G-OEG3-Mal. (D) Structure of G-actin and the site to which R6G was conjugated. The arrow in the panel indicates the sulfur atom of Cys-374, and the R6G was conjugated to this site. Molecular graphics was drawn with the UCSF Chimera package (Resource for Biocomputing, Visualization, and Informatics at the University of California, San Francisco) using published data (Protein Data Bank entry code, 4PKG [56]).

with 0.1 mM $CaCl_2$ and finally, dialysis against G-buffer (without the addition of $CaCl_2$) at 0°C. The addition of DTT to dialysis was avoided because DTT interferes the conjugation of R6G-maleimide to the Cys-374 of actin. The retentate containing G-actin was ultracentrifuged at 430,000 g for 10 min at 4°C, and the supernatant was collected.

Labeling of actin

Cys-374 of actin was labeled with the R6G maleimides according to ref [11]. G-actin solution (~1 mg/mL) was mixed to obtain final concentrations of 0.1 M KCl and 10 mM HEPES-KOH (pH 7.8), and the solution was incubated at room temperature for 30 min to allow G-actin to polymerize into F-actin. The F-actin solution was mixed with a 1.5 molar excess of R6G-maleimide over actin monomer to yield fluorescently modified actin in which R6G was conjugated to Cys-374. After the addition of DTT at a final concentration of 1 mM, the mixture was ultracentrifuged at 430,000 g for 10 min at 4°C, and the precipitate was suspended in G-buffer containing 1 mM DTT. The suspension was dialyzed against the same buffer at 0°C overnight, the retentate containing the G-actin solution was ultracentrifuged at 370,000 g for 10 min at 4°C, and then, the supernatant was collected. The fluorescent actins labeled with R6G-OEG1-Mal, R6G-OEG2-Mal, and R6G-OEG3-Mal were denoted R6G-OEG1-actin, R6G-OEG2-actin, and R6G-OEG3-actin, respectively. Contamination by free R6G dye in the fluorescently labeled actin solutions was evaluated by gel-filtration chromatography and SDS-PAGE, and such contamination was not detected. The results are described in Section S2 of the Supplementary Material.
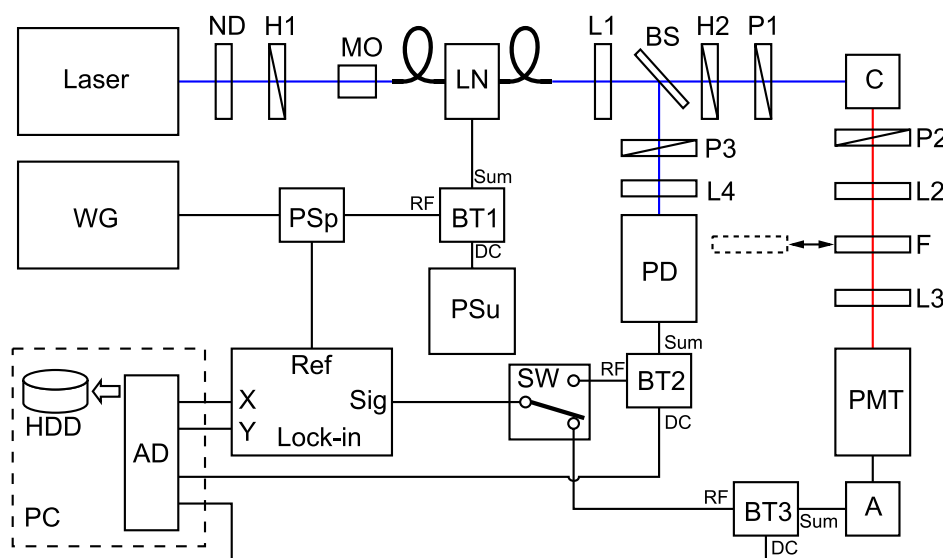
Figure 2   Block diagram of the instrumentation of the FDF measurement system. The blue lines represent the beams at 532 nm, and the red line represents the fluorescence from a sample. The thick dark curves extending from the LN are single-mode optical fibers. The other dark lines represent electronic connections. A: amplifier; AD: analog-to-digital converter; BS: beam splitter; BT1, BT2, and BT3: bias tees; C: cuvette; F: bandpass filter; H1 and H2: half waveplates; HDD: hard disk drive; L1, L2, L3, and L4: lenses; LN: lithium niobate optical modulator; MO: microscope objective; ND: neutral density filter; P1, P2 and P3: polarizers; PC: personal computer; PD: photodiode module; PMT: photomultiplier tube; PSu: DC power supply; PSp: power splitter; SW: RF switch; WG: wave generator.

Steady-state fluorescence measurements using a conventional spectrofluorometer

Steady-state fluorescence spectroscopy measurements were performed on a Fluorolog-2 spectrofluorometer (SPEX, Edison, NJ, USA). The bandpass values for the excitation and emission were 3.4 nm, the wavelength increment was 1 nm, the integration time per wavelength point was 1 sec, and the fluorescence intensity was acquired in the S/R mode. The temperature was 20°C.

Instrumentation for FDF measurements

We newly designed an instrument for FDF measurements. The measurement system consisted of sections for the modulated excitation light source, fluorescence detection, and demodulation. These three parts are described below.

Modulated excitation light source. A linearly polarized CW beam from a solid-state laser (Sapphire SF 532-50 CW CDRH; Coherent, Santa Clara, CA, USA) was focused through an ND filter (ND, Fig. 2), a half-wave plate (H1, Fig. 2), and a microscope objective (MO, Fig. 2) onto a single-mode optical fiber, which was coupled to a LN waveguide modulator (LN, Fig. 2) (AM532, JENOPTIK Optical Systems, Jena, Germany). The light emitted from the output optical fiber of the LN modulator was collimated by a lens (L1, Fig. 2), passed through a half-wave plate (H2, Fig. 2) and a Glan-Thompson prism (P1, Fig. 2) to achieve a suitable polarization angle, and then, the light was used to illuminate a cuvette (C, Fig. 2). The cuvette was connected to a circulating water bath to control the sample temperature. An ac signal (frequency, 1–200 MHz; amplitude, 0.15–0.8 V,

which was $<V_\pi$ (1.9 V) of the LN modulator) from an N5183A wave generator (WG, Fig. 2) (Agilent, Santa Clara, CA, USA) and a DC bias from a linear-regulator DC power supply (PSu, Fig. 2) were combined using a bias tee (BT1, Fig. 2) (ZFBT-4R2GW+, Minicircuits, Brooklyn, NY, USA). The combined signal (from the Sum port of the BT1, Fig. 2) was fed to the LN modulator. Thus, the LN modulator was driven using this sum signal so that the excitation light was modulated at the same frequency as the ac signal. Additionally, a portion of the modulated excitation light was separated using a beam splitter (BS, Fig. 2) and delivered to a fast-response photodiode module (PD) (HCA-S-400M-SI, FEMTO Messtechnik, Berlin, Germany). The output of the photodiode module was used to compensate for drifts in the modulated excitation light.

Fluorescence detection. When the modulated excitation light was incident on a fluorescent sample, modulated fluorescence was emitted at the same frequency as that of the ac signal. The fluorescence was passed through a polarizer plate (P2, Fig. 2) to obtain an appropriate polarization angle, a lens for collimation (L2, Fig. 2), a filter (F, Fig. 2) to block scattered light and select the fluorescence, and then, a lens (L3, Fig. 2) for projection onto a photomultiplier tube (PMT) (H10721-20MOD, Hamamatsu Photonics, Hamamatsu, Japan) that was coupled to a fast-response amplifier (A, Fig. 2) (C11184, Hamamatsu Photonics).

Data acquisition and demodulation. The outputs from the PD and PMT were both fed to bias tees (BT2 and BT3, respectively) (BT010-0S, R&K, Fuji, Japan) to split the output into signals in the high-frequency (>100 kHz) and

low-frequency (dc–kHz) ranges. The low-frequency signals from both the PMT and PD were directed to an AD converter (AD, Fig. 2) (PCI-6220, National Instruments, Austin, TX, USA) to measure their voltages. The AD converter was operated using LabVIEW software (National Instruments). The high-frequency signals were accepted by an RF switch (SW, Fig. 2) (ZX80-DR230+, Minicircuits), which in turn delivered the signals to an RF lock-in amplifier (SR844, Stanford Research Systems, Sunnyvale, CA, USA). The X and Y outputs of the lock-in amplifier were directed to the AD converter to measure signals from both the PMT and PD, where X and Y are the amplitudes of the in-phase and quadrature components, respectively, with respect to a reference wave; this terminology follows the lock-in amplifier convention. Highly shielded coaxial cables (1.5D-HQ SUPER, Fujikura, Tokyo) were used to transmit signals between the electronic devices and passive RF components.

Analysis of time-resolved fluorescence decay

As the procedure of frequency-domain fluorescence measurement, the frequency-dependent modulation depth m_f and differential phase $\Phi_{RF,f}$, which are values of sample fluorescence modulation relative to excitation light modulation [2], were calculated from the data of the FDF measurement (Section S3 of the Supplementary Material). In the present study, the fluorescence decay $f(t)$ of a sample with infinitesimally-short pulse excitation was modeled as

$$f(t) = \sum_j a_j \exp(-t/\tau_j), \tag{1}$$

where a_j is the amplitude of the exponential decay component j, and τ_j is its fluorescence lifetime. Although we devised a multi-exponential model for the fluorescence decay, hereupon, the data for both free R6G and R6G tethered to actin were described using mono-exponential functions. Theoretical expressions for the fluorescence modulation depth and differential phase are derived by the convolution of Eq 1 and the intensity of modulated excitation light expressed by

$$L(t) = p + q \cos(2\pi f t), \tag{2}$$

where p and q are constants. Accordingly, a least squares analysis was performed to determine a_j and τ_j. The least squares analysis was conducted using in-house built software that was developed in the Visual FORTRAN environment (Intel, Santa Clara, CA, USA) with a BCLSF subroutine in IMSL/MATH (Visual Numerics, Houston, TX, USA). The details of the mathematical treatments of the lifetime determination from FDF measurements are provided in Section S3 of the Supplementary Material and also in ref [2].

Analysis of time-resolved fluorescence anisotropy

In the analysis of the time-resolved fluorescence anisotropy, the modulation anisotropy and the polarization differential phase were derived from the FDF anisotropy measurement data [2]. The modulation anisotropy $r_{RF,f}$ and the polarization differential phase $\Delta\Psi_{RF,f}$ are defined as, respectively,

$$r_{RF,f} = \frac{F_{RF,VV} - G_{RF} \cdot F_{RF,VH}}{F_{RF,VV} + 2G_{RF} \cdot F_{RF,VH}}, \tag{3}$$

and

$$\Delta\Psi_{RF,f} = \Phi_{RF,VV} - \Phi_{RF,VH}, \tag{4}$$

where $\Phi_{RF,VV}$ and $\Phi_{RF,VH}$ are differential phases of the fluorescence of vertical and horizontal polarization components, respectively, with a vertically-polarized excitation light, and $F_{RF,VV}$ and $F_{RF,VH}$ are the frequency-dependent modulation amplitudes of the vertical and horizontal polarization components, respectively. The G_{RF} is a G-factor for the fluorescence modulation detection. Furthermore, the steady-state anisotropy was derived from the low-frequency components of fluorescence polarization as

$$r_{DC} = \frac{F_{DC,VV} - G_{DC} \cdot F_{DC,VH}}{F_{DC,VV} + 2G_{DC} \cdot F_{DC,VH}}, \tag{5}$$

where $F_{DC,VV}$ and $F_{DC,VH}$ are the DC components of the fluorescence intensity for the vertical and horizontal polarizations, respectively, with vertically-polarized excitation light, and G_{DC} is the G-factor in the low-frequency range (see Section S5 of the Supplementary Material). The reason of why r_{DC} given in Eq 5 corresponds to the steady-state anisotropy is explained in Section S8 of the Supplementary Material.

The time-resolved fluorescence anisotropy was modeled as a linear combination of exponential decays expressed as

$$r(t) = \sum_j r_j \exp(-t/\theta_j), \tag{6}$$

where r_j is the anisotropy decay amplitude of component j, and θ_j is its anisotropy-decay time constant. It should be noted that the sum of the anisotropy decay amplitude is the zero-time anisotropy r_0 as expressed by

$$r_0 = \sum_j r_j. \tag{7}$$

The convolution computation using the Eqs 2 and 6 gave theoretical expressions for modulation anisotropy and polarization differential phase. The theoretical expressions were fitted to the measured data to obtain the anisotropy decay amplitude r_j and the anisotropy-decay time constant θ_j for the decay component j. The details of the mathematical treatments of FDF anisotropy are provided in Section S4 of the Supplementary Material and ref [17].

Results and Discussion

Determination of the fluorescence lifetime of R6G in glycerol/water mixtures

Steady-state and frequency-domain fluorescence of R6G was examined in water/glycerol mixtures. Figure 3A shows the steady-state excitation and emission fluorescence spectra of R6G in a 5 mM HEPES-KOH buffer (pH 7.8), which exhibits spectral peaks at 525 and 552 nm, respectively, as measured by a conventional spectrofluorometer. The present
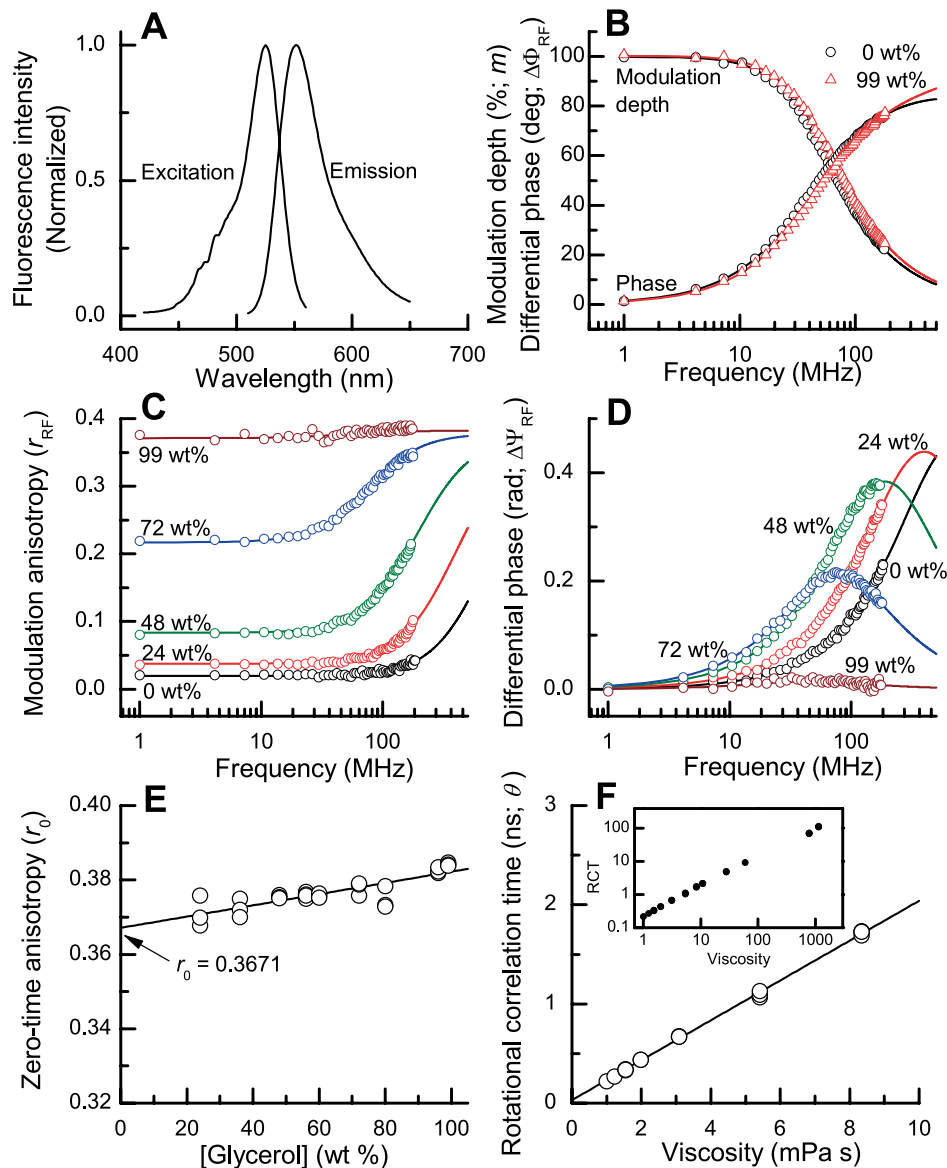
Figure 3 Fluorescence measurements of R6G in glycerol/water mixtures. (A) Fluorescence excitation and emission spectra in 5 mM HEPES-KOH (pH 7.8). The excitation spectrum was measured at an emission wavelength of 580 nm, and the emission spectrum was measured with an excitation wavelength of 500 nm. (B) FDF of R6G in (dark) 5 mM HEPES-KOH (pH 7.8) and (red) 99 wt% glycerol. (C) Modulation anisotropy of R6G in glycerol/water mixtures. The weight concentrations of glycerol are indicated in the panel. (D) Polarization differential phase of R6G. (E) Glycerol-concentration profile of the zero-time anisotropy determined by the FDF anisotropy measurement. A linear regression of the data points extrapolates to r_0=0.3671 at 0 wt% glycerol. (F) Solvent viscosity profile of the rotational correlation time of R6G below 10 mPa s. The line in the panel is drawn for guidance. Inset: Viscosity profile of the rotational correlation time of R6G over the entire viscosity range. In the panels E and F, each data point corresponds to a value derived from a single independent measurement, and three or more data points were taken at each condition. In this experiment, R6G dissolved in a 5 mM HEPES-KOH buffer (pH 7.8) was well-mixed with an appropriate weight of glycerol. The HEPES-KOH buffer was used for pH stability except for the 99 wt% glycerol solution. To prepare R6G in 99 wt% glycerol, R6G dissolved in pure water (2.7 µL) was mixed with 1000 µL of pure glycerol (purity, 99%), and the mixture was stirred well using a rotation mixer (RVM-101, Iwaki-Asahi Techno Glass, Tokyo) for more than 1 h in the dark at room temperature. The symbols in the panels are defined in the text. Excitation wavelength: 532 nm; emission wavelength: 555–615 nm; R6G concentration: 0.26 µM; temperature: 20°C.

FDF instrument (Fig. 2) provided excitation light of 532 nm and detected fluorescence emission between 555 and 615 nm through a bandpass filter; thus, the R6G fluorescence could be adequately measured by the present set-up. Figure 3B shows a plot of modulation depth and differential phase of R6G as

a function of modulation frequency in a 5 mM HEPES-KOH buffer (pH 7.8) and 99 wt% glycerol as measured by the FDF instrument. A least squares fitting analysis of the data was performed using the model function given by Eq 1, and revealed that a mono-exponential decay well described the

Table 1 Parameters of the time-resolved fluorescence of R6G in glycerol/water mixtures (mean±SE, N=3–4 for each concentration)

[Glycerol] (wt%)	Viscosity (mPa s)[a]	Steady-state anisotropy[b]	Lifetime (ns)	Analysis with unfixed r_0		Analysis with r_0 fixed to $r_{0,LR}$	
				$r_{0,UF}$	RCT (ns)	$r_{0,LR}$	RCT (ns)
0	1.002	0.0177±0.0020	3.924±0.010	N.D.	N.D.	0.3671	0.221±0.001
8	1.220	0.0226±0.0030	3.878±0.012	N.D.	N.D.	0.3683	0.271±0.001
16	1.553	0.0254±0.0026	3.891±0.010	N.D.	N.D.	0.3695	0.339±0.002
24	1.988	0.0383±0.0007	3.867±0.004	0.3712±0.0024	0.437±0.005	0.3708	0.438±0.001
36	3.088	0.0567±0.0003	3.823±0.029	0.3723±0.0014	0.676±0.004	0.3726	0.676±0.001
48	5.413	0.0846±0.0023	3.766±0.016	0.3755±0.0003	1.093±0.018	0.3744	1.097±0.015
56	8.349	0.1209±0.0005	3.750±0.002	0.3760±0.0006	1.719±0.012	0.3756	1.722±0.009
60	10.68	0.1397±0.0006	3.731±0.002	0.3758±0.0003	2.17±0.01	0.3762	2.17±0.01
72	27.62	0.2170±0.0003	3.651±0.007	0.3779±0.0010	4.88±0.03	0.3780	4.87±0.03
80	59.90	0.2720±0.0016	3.604±0.011	0.3748±0.0018	9.48±0.01	0.3792	9.55±0.05
96	780.4	0.3640±0.0006	3.494±0.004	0.3825±0.0005	71.0±0.9	0.3816	72.1±0.9
99	1150	0.3727±0.0002	3.474±0.011	0.3842±0.0003	107.7±1.8	0.3821	113.8±2.3

[a] ref [50,57]
[b] Eq 5
r_0: zero-time fluorescence anisotropy (Eqs 6, 7)
N.D.: not determined
RCT: rotational correlation time

time-resolved fluorescence of R6G in glycerol/water mixtures (glycerol concentration, 0–99 wt%) (Fig. 3B). Accordingly, the fluorescence lifetime of R6G in glycerol/water mixtures could be determined (Table 1), which was used to analyze the FDF anisotropy of R6G.

FDF anisotropy of R6G in glycerol/water mixtures and the zero-time anisotropy

The FDF anisotropy of R6G in glycerol/water mixtures was analyzed using a model function of the linear combination of exponential decays (Eq 6). Figure 3C and D shows the frequency profiles of the modulation anisotropy and polarization differential phase, respectively. Following the general property of FDF anisotropy, the modulation anisotropy approached the steady-state anisotropy value as modulation frequency decreased but approached the zero-time anisotropy value as the frequency increased. The polarization differential phase asymptotically approached zero as the modulation frequency approached zero or infinity so that the profile was bell-shaped. As can been seen in Figure 3C and D, these FDF anisotropy profiles sensitively responded to glycerol concentration or solvent viscosity.

To analyze the FDF anisotropy of R6G, the glycerol concentration range was divided into two regions of 24–99 wt% and 0–16 wt%, because the convergence of the least squares fitting varied depending on the glycerol concentration. In the higher range of 24–99 wt% glycerol, the least squares fitting was performed without fixing any parameters in Eq 6, and the time-resolved fluorescence anisotropy was described by the mono-exponential decay $r(t)=r_1 \exp(-t/\theta_1)$ (Fig. 3C and D) (for the lower range of 0–16 wt%, see below). In fact, when a bi-exponential function was tested as the model of time-resolved anisotropy, the two time constants were converged to the same value for every condition. Thereby, the

rotational correlation time (RCT) θ_1 and the zero-time anisotropy $r_0=r_1$ (See Eq 7) of R6G in glycerol/water mixtures were concurrently determined (Table 1).

The zero-time anisotropy of R6G determined thus far was found to depend on glycerol concentration. In fact, as shown in Figure 3E, the zero-time anisotropy seems to almost linearly increase with glycerol concentration. Thereby, a linear regression provides the experimentally determined zero-time anisotropy as

$$r_{0,LR} = 0.3671 + 1.5099 \times 10^{-4} \times [\text{Glyc}]_w, \qquad (8)$$

where $r_{0,LR}$ is the zero-time anisotropy derived from the linear regression, and $[\text{Glyc}]_w$ is the wt% concentration of glycerol. Steady-state anisotropy values in solvents of very high viscosity are often used as the zero-time anisotropy in time-resolved fluorescence anisotropy studies. However, the use of the steady-state anisotropy at a high viscosity would neglect solvent dependence of a fast depolarization process that depends on solvent viscosity. Thus, $r_{0,LR}$ would be a better estimation for the zero-time anisotropy than the steady-state anisotropy value at high viscosity, and, in the present analyses of FDF anisotropy, $r_{0,LR}$ was used for both free R6G and R6G tethered to actin. Table 1 shows that the RCT of R6G computed with the zero-time anisotropy fixed to $r_{0,LR}$, and the RCTs derived with unfixed r_0 and with r_0 fixed to $r_{0,LR}$ are almost the same. The slight increase of the zero-time anisotropy r_0 with glycerol concentration suggests that the fluorescence depolarization corresponding to the values of r_0 (Table 1) may arise from conformational fluctuation of R6G and the increase of the solvent viscosity may reduce the fluctuation so that r_0 increases with glycerol concentration. In fact, several dyes were reported to exhibit a decrease of r_0 value with temperature [23,24], and this may be compatible with the result presented in Figure 3E. Additionally,
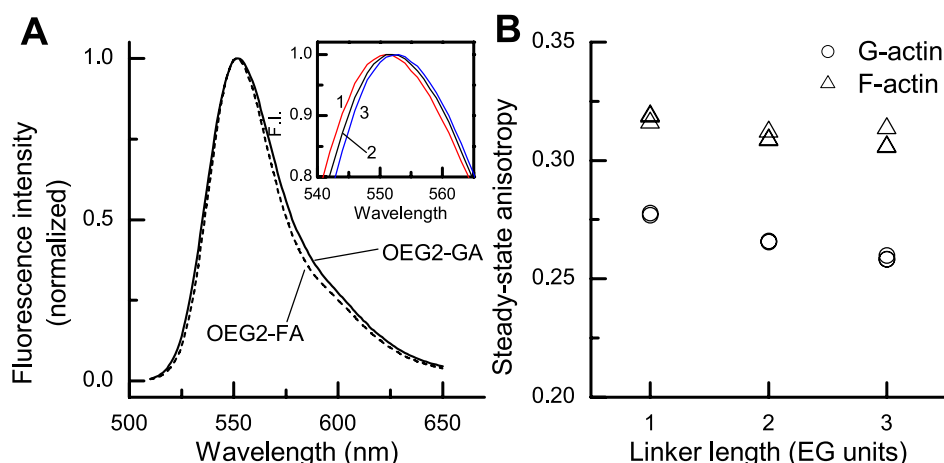
Figure 4 Steady-state fluorescence of R6G tethered to actin. (A) Fluorescence emission spectra of R6G-OEG2-G-actin and R6G-OEG2-F-actin. (Inset) Fluorescence emission spectra of R6G-OEG1-G-actin, R6G-OEG2-G-actin, and R6G-OEG3-G-actin around the emission peaks. Excitation wavelength, 500 nm. (B) Steady-state fluorescence anisotropy of R6G-OEG2-G-actin and R6G-OEG2-F-actin. In this panel, each data point corresponds to a value derived from a single independent measurement, and three or more data points were taken at each condition. Excitation wavelength: 532 nm; emission wavelength: 555–615 nm. The solution condition for G-actin was G-buffer with 0.1 mM $CaCl_2$, and that for F-actin was 0.1 M KCl, 10 mM HEPES-KOH (pH 7.8), 2 mM $MgCl_2$, and 0.2 mM ATP. For the G-actin data, the concentration of R6G-labeled G-actin was 0.25 μM. The F-actin sample was composed of 0.24 μM R6G-labeled G-actin and 6.9 μM unlabeled G-actin. The symbols in the panels are defined in the text. Temperature: 20°C.

a few studies providing values of the zero-time anisotropy of R6G have been found, but the data seemed to be somewhat scattered: 0.34 in water at 20°C [25], 0.38 in 200-Da poly(ethylene glycol) at 21°C [26], 0.380 for R6G doped in tetramethyl orthosilicate-derived sol-gels approximately 24°C [27], 0.324 in ethylene glycol by [28], and 0.372 for R6G and octadecyl-R6G in propane-1,2-diol at low temperature [29].

In the lower range of 0–16 wt% glycerol, the time-resolved fluorescence anisotropy of R6G was also described by a mono-exponential decay (Fig. 3C and D), similar to the case for the higher concentration range. In this range, it was difficult to obtain convergence in the least squares fitting computation; therefore, the fixed zero-time anisotropy values $r_{0,LR}$ were used. Accordingly, RCT θ_1 was determined as a function of glycerol concentration (Table 1). Figure 3F shows the RCT of R6G as a function of bulk solvent viscosity, demonstrating that the RCT was proportional to viscosity over the entire viscosity range. In particular, *good proportionality* was also noticed at low viscosity below 4 mPa s (inset in Fig. 3F). Thus, these results, together with the *standard errors* in Table 1, indicate that the present FDF apparatus can determine the fluorescence lifetime and RCT of R6G *precisely* and *accurately*. Additionally, the FDF anisotropy parameters were not affected by the use of 5 mM HEPES-KOH buffer (pH 7.8) instead of pure water because the lifetime and RCT of free R6G in pure water were 3.95 ns and 0.218 ns, respectively, and these values were very close to those in the presence of the 5 mM HEPES-KOH buffer (0 wt%, Table 1).

Linker length dependence of FDF anisotropy of R6G tethered to G-actin

We measured the FDF anisotropy of R6G tethered to actin through OEG linkers. R6G was connected to the Cys-374 (Fig. 1D) of actin through an amide moiety, an OEG linker, and a 3-succinimidyl propaneamide moiety in series; the OEG linker, 3-monooxapentane (OEG1), 3,6-dioxaoctane (OEG2), or 3,6,9-trioxaundecane (OEG3) was conjugated to the R6G-maleimide dyes (Fig. 1C) connected to Cys-374. This yielded three types of R6G-labeled actin molecules in which R6G was tethered to actin through linkers of three different lengths. Figure 4A shows the steady-state fluorescence emission spectrum of R6G-OEG2-G-actin in G-buffer. The peak was at 552 nm, which was the same position as that of free R6G in 5 mM HEPES-KOH buffer (pH 7.8) (Fig. 3A); therefore, the FDF of R6G-labeled actin could be measured using the same set-up that was used for free R6G in glycerol/water mixtures. Because G-buffer contained only low concentrations (≤2 mM) of solutes and the RCT of free R6G in pure water and G-buffer were measured to be 0.218 ns and 0.213 ns (data not shown), the hydrodynamic property of the G-buffer was the same as that of pure water to a good approximation. The fluorescence spectra of the R6G-labeled G-actins exhibited a modest linker-length dependence, and the order of the peak wavelengths was R6G-OEG1-G-actin < R6G-OEG2-G-actin < R6G-OEG3-G-actin (inset, Fig. 4A). The steady-state fluorescence anisotropy decreased with linker length (Fig. 4B), suggesting that the rotational mobility of R6G increases with linker length. Furthermore, the frequency-dependent modulation depth and differential phase were analyzed by least squares fitting. The
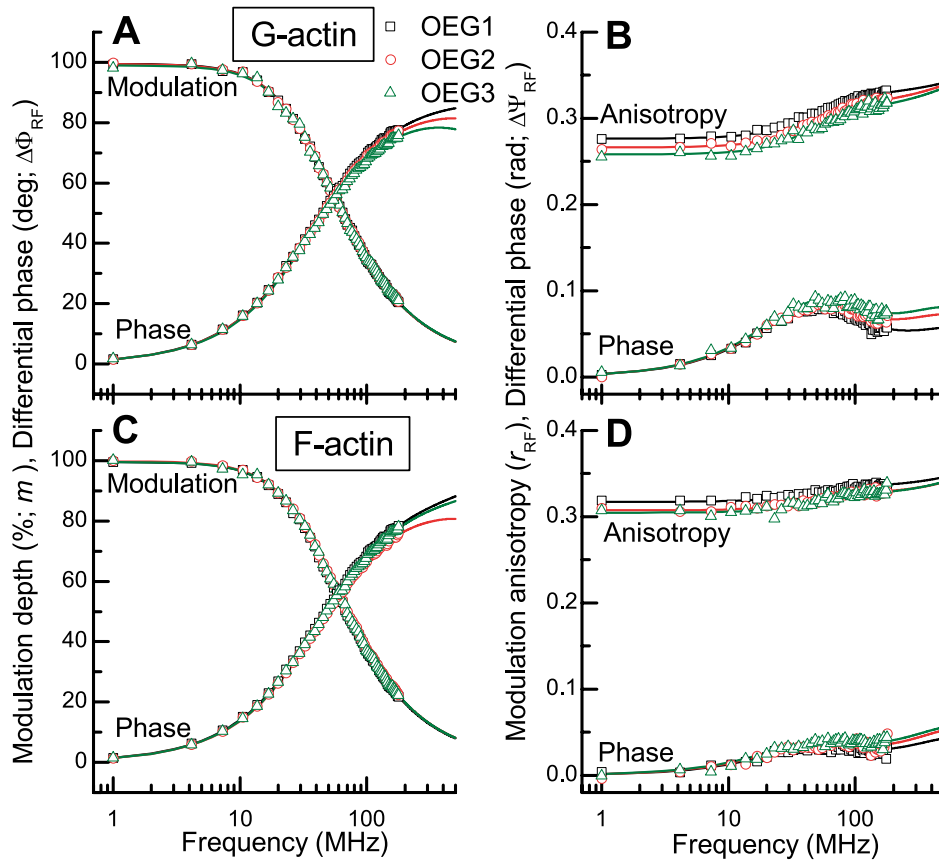
Figure 5 FDF anisotropy of R6G tethered to G-actin. (A) Modulation depth and differential phase of FDF for R6G-labeled G-actin. The solution condition was G-buffer with 0.1 mM CaCl$_2$. (B) Modulation anisotropy and polarization differential phase of R6G-labeled G-actin. (C) Modulation depth and differential phase of FDF for R6G-labeled F-actin. The solution condition was 0.1 M KCl, 10 mM HEPES-KOH (pH 7.8), 2 mM MgCl$_2$, and 2 mM ATP. (D) Modulation anisotropy and polarization differential phase of R6G-labeled F-actin. OEG1, OEG2, and OEG3 represent R6G-OEG1-actin, R6G-OEG2-actin, and R6G-OEG3-actin, respectively, and these terms apply to both G-actin and F-actin. For the G-actin data, the concentration of R6G-labeled G-actin was 0.25 μM. The F-actin sample was composed of 0.24 μM R6G-labeled G-actin and 6.9 μM unlabeled G-actin. In the panels, each data point corresponds to a value derived from a single independent measurement, and three or more data points were taken at each condition. The symbols in the panels are defined in the text. Temperature: 20°C.

analysis revealed that a mono-exponential model of fluorescence decay well described the FDF for all the three types of R6G-labeled G-actin (Fig. 5A, Table 2). Accordingly, the fluorescence lifetime of R6G tethered to actin was determined to be around 4.2 ns.

The FDF anisotropy of R6G tethered to G-actin was analyzed. For least squares fitting analysis, a linear combination of exponential decay functions given by Eq 6 was used as the model for time-resolved fluorescence anisotropy, and the zero-time anisotropy (Eq 7) was fixed at a value of $r_{0,LR}$ (Eq 8). The analysis revealed that a bi-exponential decay well described the time-resolved FDF anisotropy of R6G tethered to G-actin (Fig. 5B). The FDF anisotropy parameters derived from this analysis are shown in Table 2 and Figure 6A and B.

The fit of the bi-exponential decay to the time-resolved anisotropy indicates that the rotational motion of R6G tethered to G-actin consists of slow and fast components. The time constants of the anisotropy decay for the slow component were approximately 20 ns and changed with OEG

linker length only slightly (θ_2 in Table 2), and the anisotropy decay amplitude (r_1 and r_2) noticeably changed with OEG linker length. The time constants of anisotropy decay that were previously reported were somewhat longer than our result of 20 ns: 30 ns for G-actin labeled with dansyl or 5-({2-[(iodoacetyl)amino]ethyl}amino)naphthalene-1-sulfonic acid (IAEDANS) at 25°C [30], 45.5 ns for G-actin labeled with IAEDANS at 25°C [31], and 27.53 ns and 30.43 ns for Ca- and Mg-G-actin, respectively, with IAEDANS at 22.7°C [32]. The difference of these time constants from the present value may have occurred, probably because these studies used the zero-time anisotropy during the analyses in different manners as the present study and the use of a low zero-time anisotropy value in the least squares fitting often tends to yield a longer time constant. Incidentally, an EPR study reported a rotational correlation time of 16.0 ns for G-actin at room temperature [33], which may be somewhat nearer to our observation. Thereby, in the present study, the time constant for the slow component was assumed to be the RCT of

Table 2   Parameters of the time-resolved fluorescence of R6G tethered to G-actin and F-actin (mean±SE, N=3 for each sample)

| Sample[a]	Lifetime (ns)	Fast component[b]		Slow component[b]		Steady-state anisotropy[c]
		θ_1 (ns)	r_1	θ_2 (ns)	r_2	
R6G-OEG1-GA	4.26±0.01	0.226±0.014	0.0375±0.0005	21.4±0.2	0.330±0.001	0.2772±0.0003
R6G-OEG2-GA	4.23±0.01	0.253±0.010	0.0480±0.0002	19.8±0.3	0.319±0.001	0.2658±0.0001
R6G-OEG3-GA	4.20±0.02	0.262±0.007	0.0553±0.0007	18.7±0.3	0.312±0.001	0.2588±0.0005
R6G-OEG1-FA	3.98±0.01	0.238±0.006	0.0332±0.001	69.5±2.5	0.334±0.001	0.3178±0.0009
R6G-OEG2-FA	3.90±0.02	0.228±0.010	0.0390±0.002	55.2±1.1	0.328±0.002	0.3098±0.0012
R6G-OEG3-FA	3.90±0.01	0.287±0.030	0.0401±0.002	55.3±2.2	0.327±0.002	0.3084±0.0026

[a] GA: G-actin, FA: F-actin
[b] See Eq 6
[c] See Eq 5
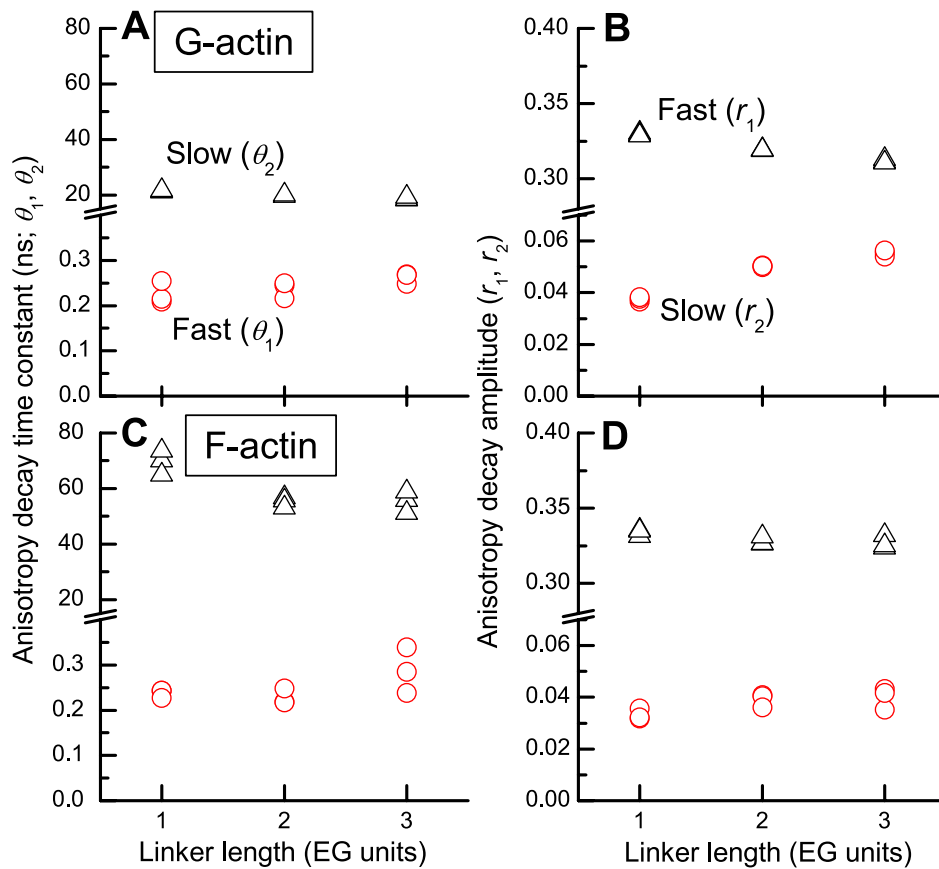
Figure 6   Linker-length dependence of FDF anisotropy parameters for R6G tethered to actin. (A) Anisotropy decay time constants of the fast and slow components for R6G tethered to G-actin. (B) Anisotropy decay amplitude of the fast and slow components for R6G tethered to G-actin. (C) Anisotropy decay time constants of the fast and slow components for R6G tethered to F-actin. (D) Anisotropy decay amplitude of the fast and slow components for R6G tethered to F-actin. The linker lengths of 1, 2, and 3 on the horizontal axis correspond to R6G-OEG1-actin, R6G-OEG2-actin, and R6G-OEG3-actin, respectively. In the panels, each data point corresponds to a value derived from a single independent measurement, and three or more data points were taken at each condition.

the tumbling motion of G-actin. The time constant for the fast component was approximately 0.2 ns (Table 2), but this value may be affected by not only the rapidity of the R6G rotational motion but also the structurally allowed range of angles.

To further evaluate the fast component of the time-resolved fluorescence anisotropy of R6G tethered to G-actin, a wobbling-in-cone model [34–36] was employed. To apply this model to R6G-labeled G-actin, we assume that (1) R6G undergoes fast wobbling motion at an RCT θ_W in an imagi-

nary cone of a semi-angle ϕ, (2) R6G-conjugated actin undergoes slow tumbling motion with an RCT θ_T, and (3) the combination of the two rotational modes is responsible for the bi-exponential decay of the fluorescence anisotropy. Thereby, we derive these rotational correlation times θ_W and θ_T from θ_1 and θ_2 (Table 2) as

$$\frac{1}{\theta_1} = \frac{1}{\theta_W} + \frac{1}{\theta_T},\tag{9}$$

and

$$\frac{1}{\theta_2} = \frac{1}{\theta_T}.\tag{10}$$

An order parameter S^2 is computed from the anisotropy decay amplitudes as follows

$$S^2 = \frac{r_2}{r_1 + r_2} = \frac{r_2}{r_0},\tag{11}$$

and the order parameter S relates to the cone-angle ϕ of the wobbling motion of R6G as

$$S = \frac{1}{2}\cos\phi(1 + \cos\phi).\tag{12}$$

The rotational diffusion coefficients (RDC) of R6G wobbling D_W and G-actin tumbling D_T are given by

$$D_W = \frac{1}{(1 - S^2)\theta_W}\left[\frac{x^2(1+x)^2}{2(x-1)}\left\{\ln\left(\frac{1+x}{2}\right) + \frac{1-x}{2}\right\}\right.$$
$$\left. + \frac{1-x}{24}(6 + 8x - x^2 - 12x^3 - 7x^4)\right],\tag{13}$$

and

$$D_T = \frac{1}{6\theta_T},\tag{14}$$

where $x = \cos\phi$. Thus, we computed the RDCs D_W and D_T and the semi-cone angle ϕ from the data shown in Table 2. Previously, the wobbling-in-cone model has been used to investigate fluorophores in membranes and micelles [34,37–39] and fluorophores bound to protein [40,41]

Figure 7 shows the OEG linker dependence of RDCs and the semi-cone angle of the wobbling motion. The result underpins the assignment of D_T to the tumbling motion of G-actin because a sphere approximation of $D_T = k_B T/8\pi\eta R^3$ for rotational diffusion yields a radius R of 2.7 and 2.6 nm for R6G-OEG1-G-actin and R6G-OEG3-G-actin, respectively, where k_B, T, η, and R are the Boltzmann constant, temperature, viscosity, and sphere radius, respectively; these R values would be comparable to the expected radius of hydrated G-actin, as actin monomer had dimensions of
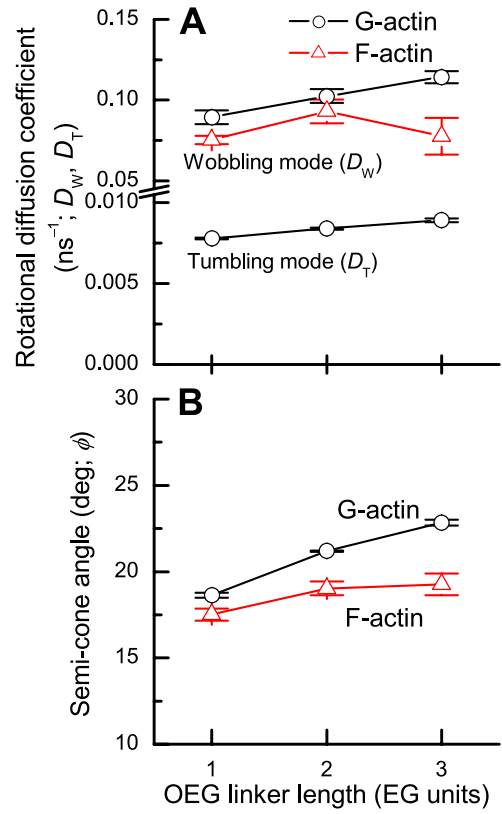

Figure 7 Linker-length dependence of the rotational motion of R6G tethered to actin derived from the wobbling-in-cone model. The data in the panels were derived from Table 2. (A) Rotational diffusion coefficients of the wobbling and tumbling modes of R6G tethered to actin. (B) Semi-cone angle of the wobbling mode of R6G tethered to G-actin and F-actin. The error bars stand for the standard errors. The symbols in the panels are defined in the text.

55 Å×55 Å×35 Å [18]. Additionally, a study of G-actin by small angle X-ray scattering reported values of 2.23 to 2.37 nm for the radius of gyration [42]. Importantly, Figure 7 shows that the values of both D_W and ϕ increase as the OEG linker length increases. This finding is most likely to be compatible with the view expected from the assumed assignment of the wobbling motion to D_W, in that the longer OEG linker is likely to lead to more rapid rotational motion and a wider semi-cone angle for the wobbling motion. Thus, in the following part of the paper, D_W is considered the RDC of the R6G wobbling motion. Previous studies found that the D_W values for fluorophores bound to host molecules were 0.018 ns^{-1} at 20°C for acrylodan covalently bound to endogenous serum albumin (ESA) [41], 0.027 ns^{-1} at 25°C for 8-anilinonaphthalene-1-sulfonate physically bound to bovine serum albumin [40], 0.12–0.26 ns^{-1} at 25°C for coumarin 153 in nanoscopic micelles [39], and 0.014–0.169 ns^{-1} at 25°C for 1,6-diphenyl-1,3,5-hexatriene in four types of membranes [37]. Among these, the situation of acrylodan covalently bound to ESA may be relatively similar to R6G tethered to G-actin, but the present D_W values for R6G (Fig.

7A) are significantly higher. This result suggests that the R6G tethered to actin examined in this study is exposed to solvent and undergoes rotational Brownian motion in the solvent phase, whereas the acrylodan bound to the Cys-34 of ESA was in the hydrophobic cleft so that the fluorophore interacted with the surrounding ESA amino acids in the cleft, leading to friction. Additionally, the RCT of the tumbling motion for free R6G in water (Table 1) gives a rotational diffusion coefficient of $1/(6\theta_1)=0.75$ ns^{-1}, which is even higher than the values of D_W for R6G tethered to G-actin (Fig. 7A). This finding suggests that the attachment of the OEG linker to R6G may act as a constraint that retards its rotational motion.

Incidentally, the use of several lengths of linkers to tether a dye to protein is useful to validate the measurement data and analysis. In fact, the FDF anisotropy data as well as the parameters derived from the analysis modestly and systematically changed with the linker length (Figs. 6 and 7). This would be plausible, because the length of the linker between actin and R6G was changed by merely one or two units of ethylene glycol (Fig. 1C). Thus, the present methodology is useful to spot an erroneous result among the whole data set.

Comparison of G-actin and F-actin

Actin is known to polymerize into actin filaments or F-actin above a physiological salt concentration [20], and we attempted to determine how the time-resolved anisotropy of R6G tethered to actin differed between G-actin and F-actin. Unlabeled G-actin and R6G-labeled G-actin were mixed at a molar ratio of 29 : 1, and this G-actin mixture underwent polymerization in the presence of 0.1 M KCl, 10 mM HEPES-KOH (pH 7.8), 2 mM MgCl$_2$, and 0.2 mM ATP at 20°C. Unlabeled G-actin was added to prevent homo-fluorescence resonance energy transfer [43] between the R6Gs bound to the same actin filaments. After incubation at 20°C for >30 min, the FDF anisotropy was measured and analyzed in a manner similar to that for G-actin. The least squares fitting analysis revealed that the time-resolved FDF of R6G tethered to F-actin was also described by a mono-exponential decay, and the time-resolved FDF anisotropy was described by a bi-exponential decay (Fig. 5C and D), irrespective of the OEG linker length. Accordingly, the derived parameters are shown in Table 2 and Figure 6C and D. As shown in Figure 6C, the anisotropy decay time constant of the slow component was above 50 ns, which is much longer than that of G-actin, but the decay time constants of the fast mode are similar to those of G-actin. However, the anisotropy decay amplitudes of the fast component r_1 for F-actin (Fig. 6D) were noticeably smaller than those for G-actin (Fig. 6B); this difference should lead to somewhat different values for the wobbling RDC, D_W. The D_W values for F-actin were slightly smaller than those for G-actin (Fig. 7A), although the OEG linker length dependence of D_W for F-actin was unfortunately unclear owing to measurement error. The semi-cone angle ϕ was concomitantly smaller for F-actin than for G-

actin (Fig. 7B). In F-actin, actin subunits contact near Cys-374 [44–46]; thus, the rotational motion of R6G tethered to F-actin may be more sterically restricted by the existence of the adjacent G-actin subunit, and this restriction may lead to a smaller ϕ. Moreover, the RDC of the R6G wobbling motion, D_W, was slightly smaller than that of G-actin, and this finding may be an indication of a difference in the dynamic properties of the solvent surrounding Cys-374 or of interactions between R6G and the actin surface. Additionally, the anisotropy decay time constants of the slow mode θ_2 for F-actin were only several-fold longer than those of G-actin (Fig. 6C). For comparison, using the average length of reconstituted actin filaments [47] and an approximate diameter of actin filament [44–46], we considered the rotational relaxation of a prolate having semi-axes of 7 nm and 1000 nm for the approximation of an actin filament in water. By a rigid prolate model [2], the rotational correlation time was calculated to be an order of 10^{-5} s. Thus, the θ_2 values of 50–80 ns measured from the present study (Fig. 6C) is considerably shorter than that expected from the tumbling motion of actin filaments. This slow component of anisotropy decay observed in the present study may suggest a composite mode of a segmental motion around the conjugation site (Cys-374) and conformational fluctuation of the OEG linker, because the time constant for the slow component changed with the OEG linker length (Fig. 6C). Previously, a study of F-actin labelled with IAEDANS, the linker of which was shorter than our OEG linkers, reported its RCTs of ~200 ns and ~400 ns for Ca^{2+}-F-actin and Mg^{2+}-F-actin, respectively, and suggested that the slow mode of the anisotropy decay reflects some restricted motion of the segments containing Cys-374 in actin filaments [48]. Another study of IAEDANS-labelled F-actin observed two slow anisotropy decay components with time constants of 900 ns and 100 ns, and the authors suggested that these time constants were attributed to motions of the regions, respectively, affected by inter-filament interaction and free from the interaction [49].

Effects of glycerol on the rotational motion of R6G tethered to G-actin

To probe the effect of the solvent surrounding G-actin on the rotational motion of R6G tethered to G-actin, the aqueous solvent was modified with a cosolvent of glycerol to measure the FDF anisotropy. R6G-labeled G-actin was dissolved in G-buffer/glycerol mixtures at concentrations of 0, 8, 16, and 24 wt%, and the FDF anisotropy was measured. Similarly to above, the analyses showed that a mono-exponential decay described the time-resolved FDF, and a bi-exponential anisotropy decay reproduced the FDF anisotropy data over the glycerol concentration range (data not shown). The anisotropy decay time constant and the RDC of G-actin tumbling were linearly shifted towards slower motion as the glycerol concentration increased (Fig. 8A, D, and G, Fig. 9A). This trend indicates the retardation of the
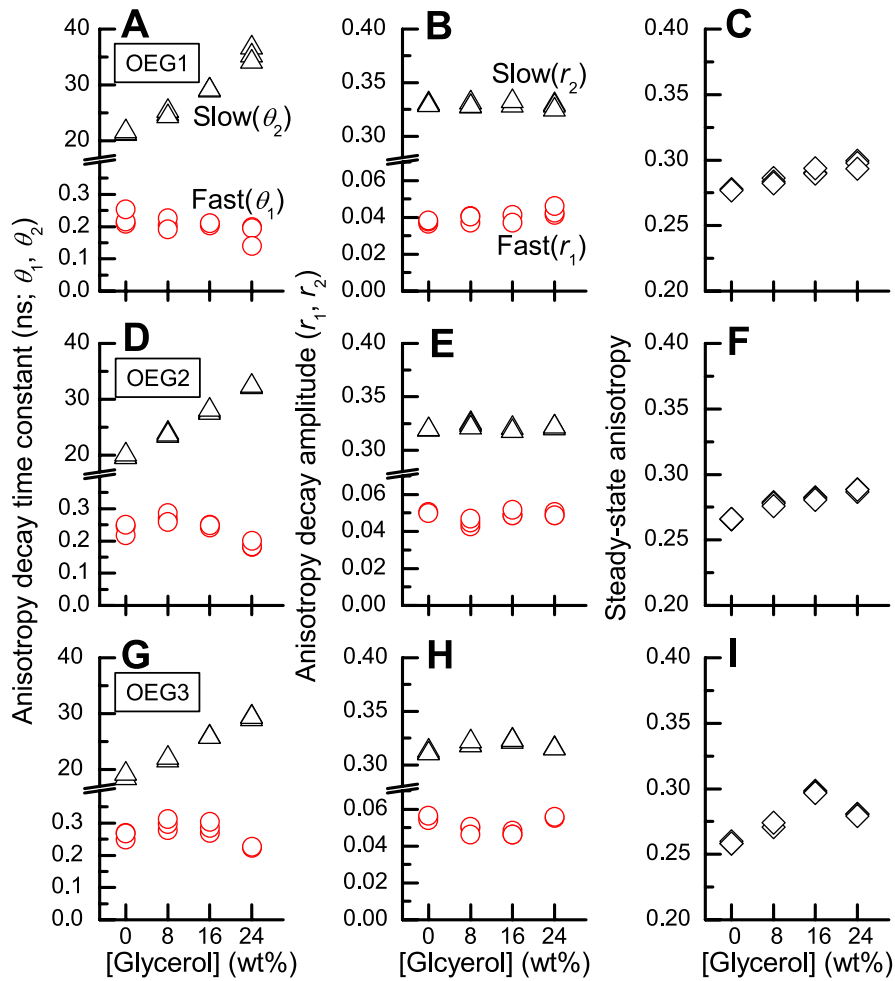
Figure 8 Glycerol concentration profiles of the anisotropy decay time constants (A, D, and G), anisotropy decay amplitude (B, E, and H), and steady-state anisotropy (C, F, and I). (A, B, and C) R6G-OEG1-G-actin. (D, E, and F) R6G-OEG2-G-actin. (G, H, and I) R6G-OEG3-G-actin. The sample solutions were prepared by mixing an appropriate weight of glycerol with an aqueous solution of 0.25 μM G-actin dissolved in G-buffer with 0.1 mM CaCl$_2$. In the panels, each data point corresponds to a value derived from a single independent measurement, and three or more data points were taken at each condition. Temperature: 20°C.

G-actin tumbling is due to an increase in solvent viscosity, because the viscosity monotonically increases with glycerol concentration [50]. The profiles of the decay time constants and decay amplitude seem to systematically change as the OEG linker length increased, i.e. the decay time constant of the fast phase for OEG3 linker (Fig. 8A, D and G) shows a peak between 8 and 16 wt% and the peak seems to systematically shift towards lower concentration as the linker length decreases. This systematic trend would be due to the modest change of the OEG linker length.

To gain insight into the rotational motion of R6G tethered to actin, the wobbling-in-cone model [34–46] was applied. In contrast to the tumbling motion, the RDC of the wobbling motion D_W for R6G-OEG1-G-actin seemed to increase with glycerol concentration and the profiles for R6G-OEG2-G-actin and R6G-OEG3-G-actin were convex downwards (Fig. 9A). These results suggest that at least in the high glycerol concentration range (≥16 wt%), R6G would be in a situation such that its wobbling motion becomes more rapid as the glycerol concentration increases. Here, it should be noted that the semi-cone angle ϕ was almost unchanged with glycerol concentration (Fig. 9B), and therefore, the steric limitation imposed on the R6G motion and the conformation of the linker portion between R6G and G-actin would be almost unchanged with the addition of glycerol. Furthermore, with reference to Figure 7A, we have suggested that the R6G tethered to G-actin substantially undergoes rotational Brownian motion in the solvent phase (see Linker length dependence of FDF anisotropy of R6G tethered to G-actin), which means that the RDC of the wobbling motion likely reflect the local viscosity of the solvent around R6G. Thus, the increase of the RDC for the wobbling motion D_W with glycerol concentration (Fig. 9A) suggests a decrease of the local viscosity of solvent around R6G tethered to actin
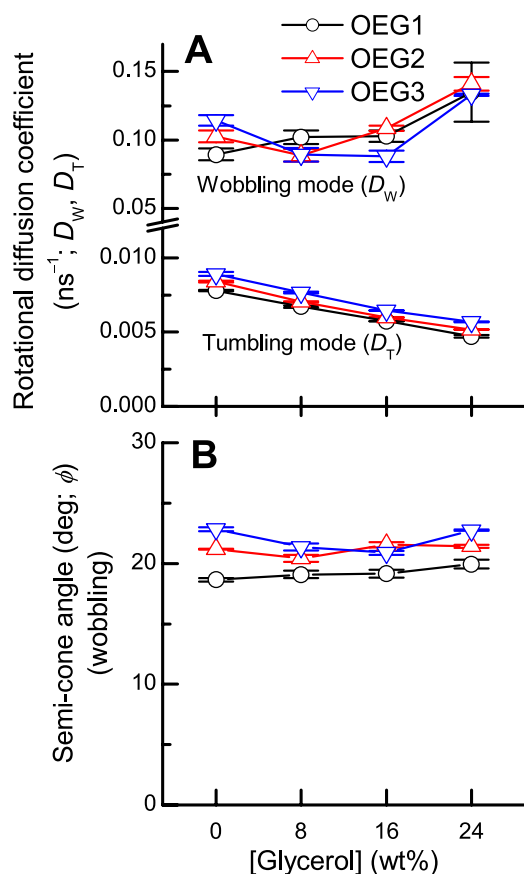
Figure 9 Glycerol concentration dependence of the rotational motion of R6G tethered to G-actin derived from the wobbling-in-cone model. The parameters were derived from the data shown in Figure 8. (A) RDC of the wobbling and tumbling modes for R6G tethered to G-actin. (B) Semi-cone angle of the wobbling mode of R6G tethered to G-actin. OEG1, OEG2, and OEG3 stand for data for R6G-OEG1-G-actin, R6G-OEG2-G-actin, and R6G-OEG3-G-actin, respectively. The error bars in the panels represent standard errors.

(up to 24 wt%), whereas the bulk viscosity of glycerol/water mixture monotonically increases with glycerol concentration [50]. This observation of the increase of RDC for the wobbling motion may be relevant to an intricate hydration effect such as the preferential solvation, in which local water concentration around a protein in the presence of glycerol is higher than the bulk [14], and the hyper-mobility of the hydration water, in which the hydration water molecules around actin exhibit higher mobility than bulk water [8,9,51]. In relation to this, the glycerol concentration dependence of the steady-state fluorescence anisotropy was unexpectedly small, and in the case of R6G-OEG3-G-actin, the anisotropy at 24 wt% was lower than that at 16 wt% (Fig. 8C, F, I). These behaviors should be compatible with the interpretation discussed above. In contrast, according to a study of the time-resolved fluorescence of rhodamine green tethered to dextran in aqueous sucrose solutions, the rotational motion of rhodamine green was monotonically slowed at increased

sucrose concentrations [52]. This result may suggest a difference between actin and dextrin in the effects of cosolvent on their solvation properties.

The result shown in Figure 9A suggests that the layer in the solvent phase surrounding R6G tethered to actin may have a local viscosity different from the bulk. The full lengths of the portion between the sulfur atom of Cys-374 of actin and R6G fluorophore are 1.6, 1.9, and 2.2 nm for R6G-OEG1-actin, R6G-OEG2-actin, and R6G-OEG3-actin, respectively. Although these linkers would not be fully extended in the aqueous solutions, the Brownian motion of R6G tethered to actin would cover regions beyond the first hydration shell of actin. Thus, the increase of D_W with glycerol concentration (Fig. 9A) may be relevant to the property of the hydration layer including regions outside the first hydration shell. Currently, hydration layer is often considered all water molecules the dynamics of which is affected by a protein molecule [53]. The RDCs of the wobbling motion (Fig. 9A) would reflect the property of such hydration layer. Previously, a terahertz spectroscopy study revealed that a dynamical hydration layer of ubiquitin covered a thickness of at least 1.8 nm on the protein surface [54]; a dielectric relaxation spectroscopy study indicated that the hydration layer around actin spanned the first to third shells of water [8].

LN modulator-based FDF method

We constructed an FDF measurement system in which single-frequency modulation of excitation light was produced by an LN modulator and the modulation frequency was swept over a range of 1–176 MHz. For FDF measurements with excitation light in the visible range, LN modulators were more useful than conventional electro-optic modulators and analogue-modulated LEDs and lasers, because LN modulators could be directly driven by common function generators at low voltages with a much faster response (>GHz) [55]. Additionally, function generators generally provide various waveforms that can be used to drive the LN modulator, and therefore, measurement modes other than single-frequency can also be performed, e.g., multiple-frequency acquisition. To the best of our knowledge, the present FDF instrument is the first time-resolved fluorescence apparatus that uses an LN waveguide modulator to produce modulated excitation light. Furthermore, if a data acquisition device that can measure a higher frequency than can the SR844 lock-in amplifier (frequency range, 25 kHz–200 MHz) is used, an FDF measurement with a single frequency mode beyond 1 GHz could be performed. Because FDF measurements can be in principle extended to time-change measurements more easily than the TCSPC method, the present technique must be valuable not only for kinetics-oriented FDF measurements but also for real-time FDF microscopy.

Conclusions

We constructed an FDF measurement system with an LN modulator that was used to generate modulated excitation light. The FDF anisotropy of free R6G in glycerol/water mixtures could be measured by the FDF system at high precision. The rotational correlation time of R6G was determined from the data using the least squares fitting analysis and was precisely proportional to the fluid viscosity of the mixtures. The FDF study of R6G tethered to G-actin through OEG linkers revealed that the time-resolved fluorescence anisotropy of R6G could be most likely ascribed to the combination of the modes of G-actin tumbling and R6G wobbling. A wobbling-in-cone model was employed to characterize the wobbling motion of R6G tethered to G-actin with two parameters: RDC and semi-cone angle. The RDC and semi-cone angle of R6G monotonically increased with OEG linker length. R6G tethered to F-actin was also investigated; the wobbling motion of R6G was slightly slower than that of G-actin, and the semi-cone angle was smaller, suggesting its sensitivity to the steric difference around the conjugation site between G-actin and F-actin. The study of R6G tethered to G-actin in glycerol/water mixtures revealed that the RDC of R6G wobbling for R6G-OEG1-G-actin monotonically increased with glycerol concentration, whereas those for R6G-OEG2-G-actin and R6G-OEG3-G-actin exhibited minima between 0 and 24 wt%. This result suggests an intricate relationship between the fluid properties of the bulk solvent and the local environment around the R6G conjugation site (Cys-374) of actin. Furthermore, the method presented in this study should be useful for investigating the properties of the local environment around the site at which a fluorescent probe attaches to a protein.

Acknowledgment

Conflict of Interest

The authors declare no competing financial interest.

Author Contributions

T. W., N. M., and M. S. directed the entire project. T. W. performed the experiments and analyzed the data. T. W., N. M., T. N., and M. S. co-wrote the manuscript.

References

[1] Steiner, R. F. Fluorescence anisotropy: Theory and applications. in *Topics in Fluorescence Spectroscopy*. (Lakowicz, J. R. ed.) vol. 2, pp. 1–52 (Springer, New York,1991).

[2] Lakowicz, J. R. *Principles of Fluorescence Spectroscopy* (Springer, New York, 2006).

[3] Bagchi, B. Water dynamics in the hydration layer around proteins and micelles. *Chem. Rev.* **105**, 3197–3219 (2005).

[4] Raschke, T. M. Water structure and interactions with protein surfaces. *Curr. Opin. Struct. Biol.* **16**, 152–159 (2006).

[5] Frauenfelder, H., Chen, G., Berendzen, J., Fenimore, P. W., Jansson, H., McMahon, B. H., *et al.* A unified model of protein dynamics. *Proc. Natl. Acad. Sci. USA* **106**, 5129–5134 (2009).

[6] Suzuki, M., Shigematsu, J. & Kodama, T. Hydration study of proteins in solution by microwave dielectric analysis. *J. Phys. Chem.* **100**, 7279–7282 (1996).

[7] Yokoyama, K., Kamei, T., Minami, H. & Suzuki, M. Hydration study of globular proteins by microwave dielectric spectroscopy. *J. Phys. Chem. B* **105**, 12622–12627 (2001).

[8] Kabir, S. R., Yokoyama, K., Mihashi, K., Kodama, T. & Suzuki, M. Hyper-mobile water is induced around actin filaments. *Biophys. J.* **85**, 3154–3161 (2003).

[9] Wazawa, T., Miyazaki, T., Sambongi, Y. & Suzuki, M. Hydration analysis of *Pseudomonas aeruginosa* cytochrome *c*551 upon acid unfolding by dielectric relaxation spectroscopy. *Biophys. Chem.* **151**, 160–169 (2010).

[10] Miyashita, Y., Wazawa, T., Mogami, G., Takahashi, S., Sambongi, Y. & Suzuki, M. Hydration-state change of horse heart cytochrome *c* corresponding to trifluoroacetic-acid-induced unfolding. *Biophys. J.* **104**, 163–172 (2013).

[11] Wazawa, T., Sagawa, T., Ogawa, T., Morimoto, N., Kodama, T. & Suzuki, M. Hyper-mobility of water around actin filaments revealed using pulse-field gradient spin-echo ^{1}H NMR and fluorescence spectroscopy. *Biochem. Biophys. Res. Commun.* **404**, 985–990 (2011).

[12] Wang, J. H. Theory of the self-diffusion of water in protein solutions. A new method for studying the hydration and shape of protein molecules. *J. Am. Chem. Soc.* **76**, 4755–4763 (1954).

[13] Halle, B. Protein hydration dynamics in solution: A critical survey. *Philos. Trans. R. Soc. Lond. B.* **359**, 1207–1224 (2004).

[14] Timasheff, S. N. Control of protein stability and reactions by weakly interacting cosolvents: The simplicity of the complicated. *Adv. Protein Chem.* **51**, 355–431 (1998).

[15] Fujiwara, S, Plazanet, M. & Oda, T. Coupling of the hydration water dynamics and the internal dynamics of actin detected by quasielastic neutron scattering. *Biochem. Biophys. Res. Commun.* **431**, 542–546 (2013).

[16] Lakowicz, J. R. & Gryczynski, I. Frequency-domain fluorescence spectroscopy. in *Topics in Fluorescence Spectroscopy* (Lakowicz, J. R. ed.) vol. 1, pp. 293–335 (Springer, New York, 1991).

[17] Lakowicz, J. R., Cherek, H., Kuśba, J., Gryczynsld, I. & Johnson, M. L. Review of Fluorescence anisotropy decay analysis by frequency-domain fluorescence spectroscopy. *J. Fluoresc.* **3**, 103–116 (1993).

[18] Dominguez, R. & Holmes, K. C. Actin structure and function. *Annu. Rev. Biophys.* **40**, 169–186 (2011).

[19] Pollard, T. D. & Cooper, J. A. Actin, a central player in cell shape and movement. *Science* **326**, 1208–1212 (2009).

[20] Straub, F. B. Actin. *Stud. Med. Chem. Univ. Szeged.* **3**, 23–37 (1943).

[21] Kaatze, U. On the existence of bound water in biological systems as probed by dielectric spectroscopy. *Phys. Med. Biol.* **35**, 1663–1681 (1990).

[22] Spudich, J. A. & Watt, S. The regulation of rabbit skeletal muscle contraction. I. Biochemical studies of the interaction of the tropomyosin-troponin complex with actin and the proteolytic fragments of myosin. *J. Biol. Chem.* **246**, 4866–4871 (1971).

[23] Zinsli, P. E. Anisotropic rotation and libration of perylene in

paraffin. *Chem. Phys.* **20**, 299–309 (1977).

[24] Viovy, J. L. Anisotropic rotation of 1,9-dimethylanthracene: A fluorescence anisotropy decay study. *J. Phys. Chem.* **89**, 5465–5472 (1985).

[25] O'hagan, W. J., McKenna, M., Sherrington, D. C., Rolinski, O. J. & Birch, D. J. S. MHz LED source for nanosecond fluorescence sensing. *Meas. Sci. Technol.* **13**, 84–91 (2002).

[26] Watkins, A. N., Ingersoll, C. M., Baker, G. A. & Bright, F. V. A parallel multiharmonic frequency-domain fluorometer for measuring excited-state decay kinetics following one-, two-, or three-photon excitation. *Anal. Chem.* **70**, 3384–3396 (1998).

[27] Narang, U., Wang, R., Prasad, P. N. & Bright, F. V. Effects of aging on the dynamics of rhodamine 6G in tetramethyl orthosilicate-derived sol-gels. *J. Phys. Chem.* **98**, 17–22 (1994).

[28] Siegel, J., Suhling, K., Lévêque-Fort, S., Webb, S. E. D., Davis, D. M., Phillips, D., *et al.* Wide-field time-resolved fluorescence anisotropy imaging (TR-FAIM): Imaging the rotational mobility of a fluorophore. *Rev. Sci. Instrum.* **74**, 182–192 (2003).

[29] Johansson, L. B-Å. Limiting Fluorescence anisotropies of perylene and xanthene derivatives. *J. Chem. Soc. Faraday Trans.* **86**, 2103–2107 (1990).

[30] Tao, T. Nanosecond fluorescence depolarization studies on actin labeled with 1,5-IAEDANS and dansyl chloride. *FEBS Lett.* **93**, 146–150 (1978).

[31] Ikkai, T., Mihashi, K. & Kouyama, T. Pulse fluorimetric study of labelled actin—DNase I complex. *FEBS Lett.* **109**, 216–218 (1980).

[32] Nyitrai, M., Hild, G., Belágyi, J. & Somogyi, B. Spectroscopic study of conformational changes in subdomain 1 of G-actin: Influence of divalent cations. *Biophys. J.* **73**, 2023–2032 (1997).

[33] Mossakowska, M., Belágyi, J. & Strzelecka-Golaszewska, H. An EPR study of the rotational dynamics of actins from striated and smooth muscle and their complexes with heavy meromyosin. *Eur. J. Biochem.* **175**, 557–564 (1988).

[34] Dutt, G. B. Are the experimentally determined microviscosities of the micelles probe dependent? *J. Phys. Chem. B* **108**, 3651–3657 (2004).

[35] Lipari, G. & Szabo, A. Effect of librational motion on fluorescence depolarization and nuclear magnetic resonance relaxation in macromolecules and membranes. *Biophys. J.* **30**, 489–506 (1980).

[36] Kinosita, K. Jr., Kawato, S. & Ikegami, A. A theory of fluorescence polarization decay in membranes. *Biophys. J.* **20**, 289–305 (1977).

[37] Kinosita, K. Jr., Kataoka, R., Kimura, Y., Gotoh, O. & Ikegami, A. Dynamic structure of biological membranes as probed by 1,6-diphenyl-1,3,5-hexatriene: A nanosecond fluorescence depolarization study. *Biochemistry* **20**, 4270–4277 (1981).

[38] Nakul, C. M., Krishna, M. M. G., Britto, P. J. & Periasamy, N. Fluorescence dynamics of dye probes in micelles. *J. Phys. Chem. B* **101**, 11051–11060 (1997).

[39] Hierrezuelo, J. M. & Ruiz, C. C. Rotational diffusion of coumarin 153 in nanoscopic micellar environments of *n*-dodecyl-β-D-maltoside and *n*-dodecyl-hexaethylene-glycol mixtures. *J. Phys. Chem. A* **116**, 12476−12485 (2012).

[40] Sahu, K., Mondal, S. K., Ghosh, S., Roy, D. & Bhattacharyya,

K. Temperature dependence of solvation dynamics and anisotropy decay in a protein: ANS in bovine serum albumin. *J. Chem. Phys.* **124**, 124909 (2006).

[41] Batabyal, S., Mondol, T. & Pal, S. K. Picosecond-resolved solvent reorganization and energy transfer in biological and model cavities. *Biochimie* **95**, 1127–1135 (2013).

[42] Sagar, A., Peddada, N., Solanki, A. K., Choudhary, V., Garg, R. & Ashish. Visualizing the elusive open shape of G-actin in solution by SAXS data analysis. *Biochem. Biophys. Res. Commun.* **435**, 740–744 (2013).

[43] Chan, F. T. S., Kaminski, C. F. & Schierle, G. S. K. HomoFRET fluorescence anisotropy imaging as a tool to study molecular self-assembly in live cells. *Chemphyschem* **12**, 500–509 (2011).

[44] Narita, A.,Oda, T. & Maeda, Y. Structural basis for the slow dynamics of the actin filament pointed end. *EMBO J.* **30**, 1230–1237 (2011).

[45] Fujii, T., Iwane, A. H., Yanagida, T. & Namba, K. Direct visualization of secondary structures of F-actin by electron cryomicroscopy. *Nature* **467**, 724–728 (2010).

[46] Oda, T., Iwasa, M., Aihara, T., Maéda, Y. & Narita, A. The nature of the globular- to fibrous-actin transition. *Nature* **457**, 441–445 (2009).

[47] Burlacu, S., Janmey, P. A. & Borejdo, J. Distribution of actin filament lengths measured by fluorescence microscopy. *Am. J. Physiol., Cell Physiol.* **262**, C569–C577 (1992).

[48] Hild, G., Nyitrai, M., Belágyi, J. & Somogyi, B. The Influence of divalent cations on the dynamic properties of actin filaments: a spectroscopic study. *Biophys. J.* **75**, 3015–3022 (1998).

[49] Ikkai, T., Wahl, P. & Auchet, J. C. Anisotropy decay of labelled actin: Evidence of the flexibility of the peptide chain in F-actin molecules. *Eur. J. Biochem.* **93**, 397–408 (1979).

[50] Haynes, W. M. *CRC Handbook of Chemistry and Physics, 95th ed.* (CRC Press, Boca Raton, 2014).

[51] Suzuki, M., Wazawa, T., Mogami, G. & Kodama, T. Role of water in actin-myosin binding and actin polymerization: the rotational and translational mobility of water molecules. *J. Physical Soc. Japan* **81**, SA003 (2012).

[52] Visser, N. V., Hink, M. A., van Hoek, A. & Visser, A. J. W. G. Comparison between fluorescence correlation spectroscopy and time-resolved fluorescence anisotropy as illustrated with a fluorescent dextran conjugate. *J. Fluoresc.* **9**, 251–255 (1999).

[53] Fogarty, A. C., Duboué-Dijon, E., Sterpone, F., Hynes J. T. & Laage, D. Biomolecular hydration dynamics: a jump model perspective. *Chem. Soc. Rev.* **42**, 5672–5683 (2013).

[54] Born, B., Kim, S. J., Ebbinghaus, S., Gruebele, M. & Havenith, M. The terahertz dance of water with the proteins: The effect of protein flexibility on the dynamical hydration shell of ubiquitin. *Faraday Discuss.* **141**, 161–173 (2009).

[55] Noguchi, K. Lithium niobate modulators. in *Broadband Optical Modulators: Science, Technology, and Applications* (Chen, A. & Murphy, E. eds.) pp. 151–172 (CRS Press, Boca Raton, 2011).

[56] Rao, J. N., Madasu, Y. & Dominguez, R. Mechanism of actin filament pointed-end capping by tropomodulin. *Science* **345**, 463–467 (2014).

[57] Segur, J. B. & Oberstar, H. E. Viscosity of glycerol and its aqueous solutions. *Ind. Eng. Chem.* **43**, 2117–2120 (1951).